

Elastic-viscoplastic anisotropic modeling of textured metals and validation using the Taylor cylinder impact test

B. Plunkett ^{a,1}, O. Cazacu ^{b,*}, R.A. Lebensohn ^c, F. Barlat ^d

^a *Air Force Research Laboratory, Munitions Directorate, Eglin AFB, FL 32542, USA*

^b *Department of Mechanical and Aerospace Engineering, University of Florida-REEF, Shalimar, FL 32579-1163, USA*

^c *Los Alamos National Laboratory, MST8, MS G755, Los Alamos, NM 87545, USA*

^d *Materials Science Division, Alcoa Inc., Alcoa Technical Center, 100 Technical Drive, Alcoa Center, PA 15069-0001, USA*

Received 18 June 2006; received in final revised form 2 October 2006

Available online 21 November 2006

Abstract

An elastic-viscoplastic model for describing the anisotropic high-strain rate behavior of both low-symmetry and high-symmetry textured materials is proposed. Yielding is described using a recently developed criterion which can capture simultaneously anisotropy and compression–tension asymmetry associated with deformation twinning. The anisotropy coefficients as well as the size of the elastic domain are considered to be functions of the accumulated plastic strain. The specific expressions for the evolution laws are determined using a multi-scale methodology, i.e. experimental measurements of crystallographic texture and uniaxial stress–strain curves, polycrystalline calculations, and macroscopic scale interpolation techniques. An overstress approach is used to incorporate rate effects in the formulation. Applications of the model to the description of the high strain-rate response of low-symmetry (hexagonal-close-packed zirconium) and high-symmetry (body-centered-cubic tantalum) pre-textured metals are presented. The very good agreement between the simulated and experimental post-test geometries of the Taylor impact specimens in terms of major and minor side profiles and impact-interface footprints shows the ability of the

* Corresponding author. Tel.: +1 850 8339350; fax: +1 850 8339366.

E-mail address: cazacu@reef.ufl.edu (O. Cazacu).

¹ Formerly Graduate Student, Department of Mechanical and Aerospace Engineering, University of Florida/REEF, United States.

model to describe with fidelity the differences in the evolution of anisotropy between zirconium and tantalum.

© 2006 Elsevier Ltd. All rights reserved.

Keywords: Anisotropic material (B); Elastic-viscoplastic material (B); Crystal plasticity (B); Impact testing (C); Finite elements (C)

1. Introduction

The importance of an adequate description of plastic anisotropy has been demonstrated in many low strain-rate forming applications (e.g. [Cazacu and Barlat, 2003](#); [Yoon et al., 2006](#); [Soare et al., in press, etc.](#)). Recent efforts in the development of computational models to describe temperature and strain-rate effects on the inelastic response have given rise to robust predictive methods for simulating the anisotropic high strain-rate behavior of body-centered-cubic (bcc) and face-centered-cubic (fcc) polycrystals. [Maudlin et al. \(1999a,b\)](#) employed an anisotropic representation of the yield surface obtained from polycrystal calculations to model the mechanical response of a pre-textured bcc tantalum sheet. [Anand et al. \(1997\)](#) developed finite-element (FE) polycrystal models for describing the high strain-rate and large deformation behavior of both bcc and fcc polycrystals. These models describe qualitatively well the important mushrooming of the Taylor impact specimens. In contrast, the prediction of the geometry changes observed in hexagonal-close-packed (hcp) specimens remains a challenge ([Maudlin et al., 1999b](#)). Metallographic investigations have shown that while deformation in hcp materials under quasi-static and dynamic loading includes both slip and deformation twinning, the propensity of twinning is higher for high-rate loading and/or low-temperature deformation. Therefore, in order to describe with accuracy the dynamic response of hcp materials it is imperative to account for the most important sources of anisotropy in the given material: slip and/or twinning activity, substructure evolution at grain level, and texture development during deformation.

Since in crystal plasticity models the distribution of crystal orientations, the available slip and/or twinning deformation systems, and the stress levels necessary to activate them are taken into account explicitly, the evolution of anisotropy due to texture development can be characterized by measuring the initial texture and calculating grain reorientation (i.e. updating the texture) using a suitable homogenization scheme. Recently, the development of crystal plasticity models for hcp metals and the incorporation of crystal plasticity calculations directly into finite element (FE) codes have received much attention. Models that account for both slip and twinning activity and employ Taylor ([Bishop and Hill, 1951](#)) or self-consistent averaging schemes ([Lebensohn and Tomé, 1993](#)) to predict the aggregate behavior have been proposed (e.g. [Staroselsky and Anand, 2003](#); [Salem et al., 2005](#); [Tomé et al., 2001](#); [Tomé and Lebensohn, 2004](#) etc.). So far, these models have been validated only for quasi-static deformation processes.

This paper presents a macroscopic elastic-viscoplastic model for describing the dynamic anisotropic plastic response of textured metals. The aim is to develop a model that can be applicable to both low-symmetry and high-symmetry pre-textured materials. Key in this development is the use of a recently proposed anisotropic yield function ([Cazacu et al., 2006](#)). This yield function (denoted in what follows as CPB06) is capable of describing

simultaneously anisotropy and tension/compression asymmetry. Moreover, if the parameter associated with strength-differential effects is set to zero, the CPB06 criterion also describes accurately the yielding of metals with no tension/compression asymmetry.

The plan of the paper is as follows. Section 2 presents an overview of the proposed elastic-viscoplastic model. In Section 3, numerical aspects related to the FE implementation of the model are discussed. In Section 4 we present an application of the proposed formulation to hcp materials. In particular, we describe how the parameters involved in the evolution laws for a high-purity zirconium clock-rolled plate can be determined, based on experimental information (texture, quasi-static uniaxial tension and compression loading curves and metallographic evidence) and simulation results obtained with the viscoplastic self-consistent (VPSC) polycrystalline model of [Lebensohn and Tomé \(1993\)](#). Next, a validation of the anisotropic low strain-rate formulation is provided by comparing FE simulations with experimental results on the zirconium plate. The elastic-viscoplastic extension of the model is then used to simulate Taylor cylinder impact test results for the same material. We conclude with an application of the model to bcc materials performing the analysis of the Taylor cylinder impact test on pre-textured tantalum. It is shown that the model describes with accuracy the striking difference between the geometries of the post-test specimens of zirconium and tantalum.

2. Anisotropic elastic-viscoplastic model

Our objective is to develop a macroscopic anisotropic model that describes simultaneously the influence of strain-rate, temperature, and evolving texture on the inelastic response of textured metals for monotonic loading paths. Thus, an elastic/viscoplastic approach (see [Perzyna, 1966](#)) is adopted. The basic assumption is that the viscous properties of materials become manifest only after the passage to the plastic state. Thus, the strain-rate $\dot{\epsilon}$ can be decomposed additively into an elastic part ($\dot{\epsilon}_E$) and a viscoplastic part ($\dot{\epsilon}_{vp}$), the latter representing the combined viscous and plastic effects, i.e.

$$\dot{\epsilon} = \dot{\epsilon}_E + \dot{\epsilon}_{vp} \quad (1)$$

The evolution of the viscoplastic strain-rate is considered to be given by an overstress type law of the form:

$$\dot{\epsilon}_{vp} = \gamma \langle \phi(f) \rangle \frac{\partial g}{\partial \sigma} \quad (2)$$

where

$$\langle \phi(f) \rangle = \begin{cases} 0 & \text{for } f \leq 0, \\ f^m & \text{for } f > 0. \end{cases} \quad (3)$$

In Eq. (2), f is the quasi-static yield function, g is the quasi-static plastic potential, γ a viscosity parameter, and m is a strain-rate sensitivity constant.

The overstress law (2) reduces to the classic plastic flow rule if the strain rate goes to zero ([Perzyna, 1966](#)). The quasi-static yield function is the CPB05 yield function ([Cazacu et al., 2006](#)):

$$f(\sigma, \bar{\epsilon}_{vp}, T) = \frac{\bar{\sigma}(\sigma, \bar{\epsilon}_{vp})}{Y(\bar{\epsilon}_{vp}, T)} - 1 \quad (4)$$

where Y is a hardening parameter, which is a function of the accumulated equivalent viscoplastic strain $\bar{\epsilon}_{vp}$, and, possibly, of the temperature T , while $\bar{\sigma}$ is an equivalent stress defined in the CPB05 framework as (Cazacu et al., 2006; Plunkett et al., 2006):

$$\bar{\sigma} = B[(|\Sigma_1| - k\Sigma_1)^a + (|\Sigma_2| - k\Sigma_2)^a + (|\Sigma_3| - k\Sigma_3)^a]^{\frac{1}{a}} \quad (5)$$

with B being a constant defined such that $\bar{\sigma}$ reduces to the tensile yield stress in the rolling direction, i.e.

$$B = \left[\frac{1}{(|\Phi_1| - k\Phi_1)^a + (|\Phi_2| - k\Phi_2)^a + (|\Phi_3| - k\Phi_3)^a} \right]^{\frac{1}{a}} \quad (6)$$

and

$$\begin{aligned} \Phi_1 &= \left(\frac{2}{3}L_{11} - \frac{1}{3}L_{12} - \frac{1}{3}L_{13} \right); & \Phi_2 &= \left(\frac{2}{3}L_{12} - \frac{1}{3}L_{22} - \frac{1}{3}L_{23} \right); \\ \Phi_3 &= \left(\frac{2}{3}L_{13} - \frac{1}{3}L_{23} - \frac{1}{3}L_{33} \right) \end{aligned} \quad (7)$$

In Eq. (5), $\Sigma_1, \Sigma_2, \Sigma_3$ are the principal values of the tensor $\Sigma = \mathbf{L}[S]$, where \mathbf{L} is a fourth-order orthotropic tensor that accounts for the plastic anisotropy of the material and \mathbf{S} is the deviator of the Cauchy stress tensor, k is a strength-differential parameter, and a is a homogeneity constant. Note that for the case of $a = 2$, $k = 0$, and \mathbf{L} equal to the fourth-order identity tensor, CPB05 reduces to the von Mises criterion and B reduces to $\sqrt{3}/2$, i.e. the constant associated with the von Mises effective stress. The effective plastic strain associated with this anisotropic yield function is calculated using the principle of equivalence of plastic work (Hill, 1987).

In the above equations all stresses and strains are expressed in a materially embedded coordinate system such as to ensure that the resulting incremental constitutive law is objective (Yoon et al., 1999). The evolution of anisotropy due to evolving texture is accounted for by means of a multi-scale procedure, which essentially consists in using experimental textures and stress–strain curves, polycrystalline calculations, and macroscopic scale interpolation techniques. The procedure starts by fitting the parameters of a polycrystal model (we use the VPSC formulation) to reproduce the mechanical response of the pre-textured material along a given deformation path (note that the measured initial texture is needed as input of the polycrystal model). Specifically, using VPSC, the polycrystal is pre-strained up to a given deformation level $\bar{\epsilon}_{vp}^j$ along a given deformation path. Then, in order to quantify the induced anisotropy, the pre-strained polycrystal is further “numerically” probed along various directions. The calculated yield stresses along these various test directions are in turn used to determine the coefficients $\mathbf{L}(\bar{\epsilon}_{vp}^j), k(\bar{\epsilon}_{vp}^j), a(\bar{\epsilon}_{vp}^j)$ involved in the macroscopic CPB05 yield criterion and thus to obtain the macroscopic yield surface corresponding to the texture for the given level of pre-strain, by calculating $\bar{\sigma}^j$ according to Eq. (5), as well as $Y^j = Y(\bar{\epsilon}_{vp}^j)$. This procedure is repeated for a finite set of pre-strain levels, say $\bar{\epsilon}_{vp}^1 < \bar{\epsilon}_{vp}^2 < \dots < \bar{\epsilon}_{vp}^n$. Further, an interpolation procedure is used to obtain the macroscopic yield surfaces corresponding to any pre-strain level (Plunkett et al., 2006), i.e.

$$\bar{\sigma}(\boldsymbol{\sigma}, \bar{\epsilon}_{vp}) = \xi(\bar{\epsilon}_{vp})\bar{\sigma}^j + [1 - \xi(\bar{\epsilon}_{vp})]\bar{\sigma}^{j+1} \quad (8a)$$

$$Y(\bar{\epsilon}_{vp}, T) = \xi(\bar{\epsilon}_{vp}) \cdot Y^j + (1 - \xi(\bar{\epsilon}_{vp})) \cdot Y^{j+1} \quad (8b)$$

for any $\bar{\epsilon}_{vp}^j \leq \bar{\epsilon}_{vp} \leq \bar{\epsilon}_{vp}^{j+1}$, $j = 1 \dots n - 1$. The interpolation parameter $\xi(\bar{\epsilon}_{vp})$ appearing in Eq. (8) is defined as

$$\xi(\bar{\epsilon}_{vp}) = \frac{\bar{\epsilon}_{vp}^{j+1} - \bar{\epsilon}_{vp}}{\bar{\epsilon}_{vp}^{j+1} - \bar{\epsilon}_{vp}^j} \tag{9}$$

It is worth noting that, although the above procedure delivers a viscoplastic response for any applied state at any accumulated deformation, such mechanical response represents a good approximation of the actual behavior of the material only for applied loadings with moderate deviations with respect to the adopted pre-strain deformation path. For quasi-static strain rates, the proposed elastic/viscoplastic model reduces to an elastic/plastic model (see Perzyna, 1966).

3. Integration algorithm

In order to simulate high-rate deformation processes, the elastic-viscoplastic model described by Eqs. (1)–(7), (8a), (8b) was implemented in the commercial FE code ABAQUS (2003). The algorithmic aspects related to the FE implementation are presented in what follows.

In displacement-based FE formulations, stress updates take place at the Gauss points for a prescribed nodal displacement. We start from the known converged state $[\boldsymbol{\epsilon}^t, \boldsymbol{\epsilon}'_{vp}, \boldsymbol{\sigma}^t, \bar{\epsilon}'_{vp}]$ and calculate the corresponding values at $t + \Delta t$: $[\boldsymbol{\epsilon}^{t+\Delta t}, \boldsymbol{\epsilon}'_{vp}, \boldsymbol{\sigma}^{t+\Delta t}, \bar{\epsilon}'_{vp}]$. In this incremental process, the total strain increment $\Delta \boldsymbol{\epsilon}$ is decomposed into an elastic part $\Delta \boldsymbol{\epsilon}_E$ part and a viscoplastic part $\Delta \boldsymbol{\epsilon}_{vp}$ according to:

$$\Delta \boldsymbol{\epsilon} = \Delta \boldsymbol{\epsilon}_E + \Delta \boldsymbol{\epsilon}_{vp} \tag{10}$$

The stress increment is related to the elastic strain by Hooke’s law

$$\Delta \boldsymbol{\sigma} = \mathbf{C} : \Delta \boldsymbol{\epsilon}_E = \mathbf{C} : (\Delta \boldsymbol{\epsilon} - \Delta \boldsymbol{\epsilon}_{vp}) \tag{11}$$

where \mathbf{C} is the fourth-order stiffness tensor. Next, a trial elastic stress: $\boldsymbol{\sigma}_{trial} = \boldsymbol{\sigma}^t + \mathbf{C}:\Delta \boldsymbol{\epsilon}$ is calculated. If $f(\boldsymbol{\sigma}_{trial}, \bar{\epsilon}_{vp}, T) \leq 0$, the increment is elastic and $\boldsymbol{\sigma}^{t+\Delta t} = \boldsymbol{\sigma}_{trial}$. If $f(\boldsymbol{\sigma}_{trial}, \bar{\epsilon}_{vp}, T) > 0$, then there is viscoplastic flow and the stress update is obtained by estimating the viscoplastic strain increment $\Delta \boldsymbol{\epsilon}_{vp}$ (Simo and Hughes, 1998). A fully implicit integration scheme was used, i.e. the viscoplastic flow was determined by the gradient of the potential function at $t + \Delta t$:

$$\Delta \boldsymbol{\epsilon}_{vp} = \Delta \dot{\boldsymbol{\epsilon}}_{vp}^{t+\Delta t} \Delta t = \gamma \langle \phi^{t+\Delta t} \rangle \Delta t \left(\frac{\partial \bar{\sigma}}{\partial \boldsymbol{\sigma}} \right)_{t+\Delta t} \tag{12}$$

Next, Eq. (12) is cast into the following form (Wang et al., 1997):

$$\Delta \boldsymbol{\epsilon}_{vp} = \Delta h \left(\frac{\partial \bar{\sigma}}{\partial \boldsymbol{\sigma}} \right)_{t+\Delta t} \tag{13}$$

where the multiplier Δh was introduced under the constraint that the residual Δr given by:

$$\Delta r = \frac{\Delta h}{\gamma \Delta t} - \phi(\boldsymbol{\sigma}^{t+\Delta t}, h^{t+\Delta t}, T) \tag{14}$$

tends to zero upon convergence of a local iterative procedure. Since the effective stress $\bar{\sigma}$ is homogeneous of degree one in stresses, $\Delta \bar{\epsilon}_{vp} = \Delta h$. Substituting Eq. (13) into Eq. (11) yields:

$$\Delta\boldsymbol{\sigma} = \mathbf{C} : \left(\Delta\varepsilon - \Delta h \left(\frac{\partial \bar{\sigma}}{\partial \boldsymbol{\sigma}} \right)_{t+\Delta t} \right) \tag{15}$$

To compute Δh , a Taylor expansion of the residual is considered around its value at the previous local iteration, i.e.:

$$r_{n+1}^{t+\Delta t} \approx r_n^{t+\Delta t} + \left[\frac{\partial r}{\partial \Delta h} \right]_n^{t+\Delta t} \delta h_{n+1} + \left[\frac{\partial r}{\partial \boldsymbol{\sigma}} \right]_n^{t+\Delta t} : \delta \boldsymbol{\sigma}_{n+1} + \left[\frac{\partial r}{\partial T} \right]_n^{t+\Delta t} \delta T_{n+1} \approx 0 \tag{16}$$

where n is a counter for the local iteration ($n = 0$ denotes the trial elastic state), $\delta h_{n+1} = \Delta h_{n+1} - \Delta h_n$, $\delta \boldsymbol{\sigma}_{n+1} = \Delta \boldsymbol{\sigma}_{n+1} - \Delta \boldsymbol{\sigma}_n$, and $\delta T_{n+1} = \Delta T_{n+1} - \Delta T_n$. Replacing Eq. (14) in Eq. (16) we obtain (omitting supra-indices):

$$r_{n+1} \approx r_n + \frac{1}{\gamma \Delta t} \delta h_{n+1} - \left[\frac{\partial \varphi}{\partial \boldsymbol{\sigma}} \right]_n \delta \boldsymbol{\sigma}_{n+1} - \left[\frac{\partial \varphi}{\partial h} \right]_n \delta h_{n+1} - \left[\frac{\partial \varphi}{\partial T} \right]_n \delta T_{n+1} \approx 0 \tag{17}$$

The stress update for the trial state ($n = 0$) is found by assuming that the total strain increment was elastic, while for $n > 0$, the variation of $\Delta \boldsymbol{\sigma}$ can be determined by considering the effect of the viscoplastic strain on the state of stress as

$$\delta \boldsymbol{\sigma}_{n+1} = -\mathbf{C} : \delta h_{n+1} \left[\frac{\partial \bar{\sigma}}{\partial \boldsymbol{\sigma}} \right]_{n+1} \tag{18}$$

The term $\left[\frac{\partial \bar{\sigma}}{\partial \boldsymbol{\sigma}} \right]_{n+1}$ may be approximated by:

$$\left[\frac{\partial \bar{\sigma}}{\partial \boldsymbol{\sigma}} \right]_{n+1} \approx \left[\frac{\partial \bar{\sigma}}{\partial \boldsymbol{\sigma}} \right]_n + \Theta \left\{ \left[\frac{\partial^2 \bar{\sigma}}{\partial \boldsymbol{\sigma}^2} \right]_n : \delta \boldsymbol{\sigma}_{n+1} + \left[\frac{\partial^2 \bar{\sigma}}{\partial h \partial \boldsymbol{\sigma}} \right]_n \delta h_n \right\} \tag{19}$$

where Θ ($0 \leq \Theta \leq 1$) is an interpolation parameter. Combining Eqs. (18) and (19):

$$\delta \boldsymbol{\sigma}_{n+1} = -H : \left[\left(\frac{\partial \bar{\sigma}}{\partial \boldsymbol{\sigma}} \right)_n + \Theta \delta h_n \left(\frac{\partial^2 \bar{\sigma}}{\partial h \partial \boldsymbol{\sigma}} \right)_n \right] \delta h_{n+1} \tag{20}$$

where

$$\mathbf{H}^{-1} = \mathbf{C}^{-1} + \Theta \delta h_n \frac{\partial^2 \bar{\sigma}}{\partial \boldsymbol{\sigma}^2} \tag{21}$$

Further substitution of Eq. (20) into Eq. (17) yields

$$\delta h_{n+1} = \frac{1}{\beta} \left[r_n + \left(\frac{\partial \varphi}{\partial T} \right)_n \delta T_{n+1} \right] \tag{22}$$

with

$$\beta = \left(\frac{\partial \varphi}{\partial \boldsymbol{\sigma}} \right) : H : \left[\left(\frac{\partial \bar{\sigma}}{\partial \boldsymbol{\sigma}} \right)_n + \Theta \delta h_n \frac{\partial^2 \bar{\sigma}}{\partial h \partial \boldsymbol{\sigma}} \right] - \frac{\partial \varphi}{\partial h} + \frac{1}{\gamma \Delta t} \tag{23}$$

In Eq. (22) note that, since the total strain increment is fixed during the local iterative procedure, $\delta \varepsilon_{n+1} = 0$. The derivatives appearing in the above equations are calculated based on the flow rule (see Eq. (2)):

$$\frac{\partial \phi}{\partial \sigma} = m \left(\frac{\bar{\sigma}}{Y} - 1 \right)^{m-1} \frac{1}{Y} \frac{\partial \bar{\sigma}}{\partial \sigma} \quad (24a)$$

$$\frac{\partial \phi}{\partial h} = m \left(\frac{\bar{\sigma}}{Y} - 1 \right)^{m-1} \left(\frac{1}{Y} \frac{\partial \bar{\sigma}}{\partial \bar{\epsilon}_{vp}} - \frac{\bar{\sigma}}{Y^2} \frac{\partial Y}{\partial \bar{\epsilon}_{vp}} \right) \quad (24b)$$

$$\frac{\partial \phi}{\partial T} = -m \left(\frac{\bar{\sigma}}{Y} - 1 \right)^{m-1} \frac{\bar{\sigma}}{Y^2} \frac{\partial Y}{\partial T} \quad (24c)$$

4. Results

4.1. Quasi-static deformation of zirconium

In this section and the following we present applications of the proposed model to high-purity zirconium. Results of uniaxial compression tests on a clock-rolled zirconium plate were reported by Maudlin et al. (1999b), Kaschner and Gray (2000), and Tomé et al. (2001). This hcp aggregate is highly anisotropic, both at single crystal and polycrystal levels. It was processed through a series of clock-rolling and annealing cycles to produce a plate with strong basal texture ($\langle c \rangle$ -axes of the hcp crystals predominantly oriented along the plate normal direction). The process of multiple rolling passes with rotation was used in order to obtain a nearly isotropic in-plane texture. Let (x, y, z) be a coordinate reference frame associated with the plate, where the (x, y) plane corresponds to the original rolling plane, while the z -direction is the through-thickness (TT) direction. Right-circular cylindrical tests specimens were cut from the plate both in the TT (z -) and in-plane (IP) (x - or y -) directions. Quasi-static tests in both IP and TT directions were carried out at room temperature (298 K) and liquid nitrogen temperature (77 K) (Tomé et al., 2001). In this paper we will restrict our analysis to room temperature results. It was found that the mechanical response is highly dependent on the predominant orientation of the $\langle c \rangle$ -axis with respect to the loading direction (Tomé et al., 2001). The large variations observed in flow stress and strain-hardening rate are due to the relative orientation of the available twinning and slip systems and the critical stress levels required to activate them. In the case of TT samples, the loading is applied parallel to the predominant $\langle c \rangle$ -axis orientation. Deformation along the $\langle c \rangle$ -axis requires the activation of $\{10\bar{1}2\}\langle 10\bar{1}\bar{1} \rangle$ tensile twinning, $\{10\bar{1}1\}\langle \bar{1}\bar{1}23 \rangle$ pyramidal $\langle c + a \rangle$ -slip or the much harder $\{11\bar{2}2\}\langle 11\bar{2}\bar{3} \rangle$ compressive twinning. Analysis of the activity of these deformation systems with the VPSC model shows that at room temperature tensile twinning and pyramidal $\langle c + a \rangle$ -slip dominate in tension and compression along the $\langle c \rangle$ -axis, respectively (see Fig. 6 in Tomé et al., 2001), although some minor activity of $\{11\bar{2}2\}\langle 11\bar{2}\bar{3} \rangle$ compressive twinning and $\{11\bar{2}1\}\langle 11\bar{2}\bar{6} \rangle$ tensile twinning has been also observed (Henrie et al., 2004). In the case of IP samples, the material can deform within the plane without having much change in dimension along the harder-to-deform $\langle c \rangle$ -axis. Plastic flow occurs at lower applied stresses because $\{10\bar{1}0\}\langle \bar{1}2\bar{1}0 \rangle$ prismatic slip and tensile twinning are easily activated (see also Fig. 6 of Tomé et al. (2001), which shows the evolution of the relative activity of deformation modes and twin fractions with deformation, for TT and IP samples).

In what follows, all the reported numerical tests using the VPSC model were carried out assuming: (a) the experimental initial texture (consisting of 377 orientations) of the clock-rolled zirconium plate, (b) the deformation mechanisms characterized operational at room

temperature (i.e. prismatic $\langle a \rangle$ -slip, pyramidal $\langle c + a \rangle$ -slip and tensile twinning), and (c) the values of the slip and twinning parameters (critical stresses, hardening coefficients, and rate sensitivity exponent), as reported by Tomé et al. (2001). Comparison between the experimental textures and textures predicted with the VPSC model were provided in the same paper.

As already mentioned, in order to experimentally characterize the anisotropy induced by texture evolution, the material should be subjected to a specific loading, up to pre-determined deformation levels. The choice of the pre-strain loading direction should be consistent with the main deformation path that the aggregate will undergo in a specific application (e.g. uniaxial compression for Taylor impact testing). Then, specimens should be cut from the pre-strained sample and further tests performed to quantify the anisotropy induced by deformation. However, this would require a large number of mechanical tests, which could be very difficult to carry out. Indeed, there is little data for large-strain in-plane compression of Zr in sheet form because measurements are limited by buckling. Alternatively, the evolution of the yield surface can be studied by performing numerical tests using VPSC model. For the clock-rolled plate of zirconium described previously, the VPSC code was first used to characterize the evolution of the yield surface during IP compression. For this purpose, the polycrystal was pre-strained up to given deformation levels. Fig. 1 shows the biaxial stress plane projections of the VPSC yield loci (symbols) corresponding to pre-strain levels of $\bar{\epsilon}_{vp}^1 = 0.2\%$, $\bar{\epsilon}_{vp}^2 = 1\%$, $\bar{\epsilon}_{vp}^3 = 5\%$, $\bar{\epsilon}_{vp}^4 = 25\%$, $\bar{\epsilon}_{vp}^5 = 35\%$, $\bar{\epsilon}_{vp}^6 = 45\%$, and $\bar{\epsilon}_{vp}^7 = 60\%$. Next, for each individual pre-strain level we obtained $\bar{\sigma}^j$ and determined the coefficients $L(\bar{\epsilon}_{vp}^j)$, $k(\bar{\epsilon}_{vp}^j)$, $a(\bar{\epsilon}_{vp}^j)$ (using 36 data points calculated with VPSC and a least-square fitting procedure in conjunction with Eqs. (5)–(7)) and $Y^j = Y(\bar{\epsilon}_{vp}^j)$ as well. The homogeneity parameter was considered to have a fixed value $a = 2$ because of the nearly elliptical shape of the yield loci for high-purity zirconium. This procedure was repeated for all seven pre-strain levels. The numerical values of these coefficients for each CPB06 yield surface are listed in Table 1. These coefficients quantify the very strong plastic anisotropy for this material and its strong evolution with strain. Also, the linear interpolation

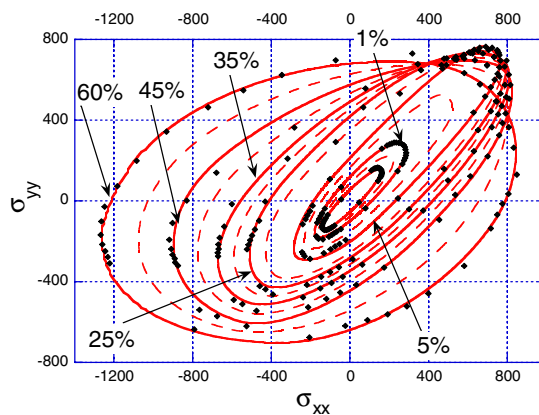


Fig. 1. Theoretical yield surface evolution for a zirconium clock-rolled plate during in-plane compression for various levels of pre-strain. Solid lines: CPB06 yield surfaces corresponding to fixed pre-strain levels, determined using the VPSC code (symbols). Dashed lines: CPB06 yield surfaces for intermediate pre-strain levels obtained by linear interpolation.

Table 1

CPB06 yield function coefficients corresponding to various pre-strain levels for uniaxial compression of clock-rolled zirconium along an in-plane direction

	k	L_{12}	L_{13}	L_{22}	L_{23}	L_{33}	L_{44}	L_{55}	L_{66}
0.2%	0.071	2.883	1.875	1.252	1.965	1.204	0.989	1.075	3.956
1%	0.224	2.15	1.407	1.179	1.438	0.892	0.604	0.617	1.691
5%	0.500	2.923	1.823	0.865	1.745	0.418	0.984	1.145	2.980
25%	0.263	2.704	1.727	1.821	2.056	0.869	0.949	0.791	1.403
35%	0.174	2.505	1.683	2.320	2.054	1.012	0.889	0.694	1.098
45%	-0.269	0.853	1.444	1.143	0.624	1.007	0.638	0.461	0.665
60%	-0.220	0.766	0.858	0.637	0.900	0.644	0.299	0.189	0.255

For all levels of effective plastic strain: $a = 2$ and $L_{11} = 1.0$

procedure was used to obtain the macroscopic yield surfaces corresponding to any pre-strain level (see Eq. (8)). In Fig. 1, the dashed lines represent the CPB06 yield surfaces for intermediate pre-strain levels obtained using linear interpolation. Note that an accurate description of the evolving yield function for pre-strain levels of around 30% and, further, up to 60% are needed for the quasi-static IP compression simulation below, and for the Taylor cylinder simulation of next subsection, respectively. It is also worth mentioning that the successive yield function projections for pre-strains higher than 5% are more rounded and centered, reflecting a decrease of the plastic anisotropy (note that all anisotropy coefficients have initially rather large values which decrease at large strains). This effect is related to the high tensile twinning activity and the concomitant strong reorientation of the twinned portions of the grains that take place during in-plane compression.

The proposed model was used to simulate the quasi-static uniaxial compression of a right cylinder of circular cross section with its axis parallel to the in-plane x -direction up to 28% longitudinal strain, for comparison with analog experimental results reported by Tomé et al. (2001) (Fig. 2). Note that because the z -direction is very hard to deform,

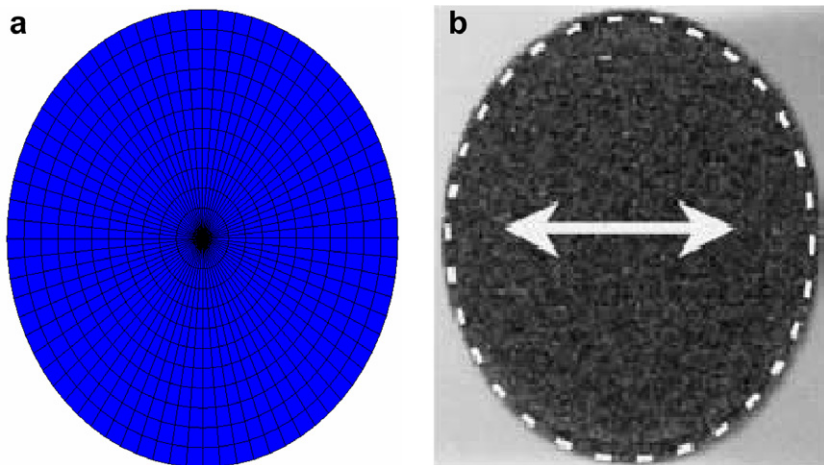


Fig. 2. Cross-sections for quasi-static compression of a zirconium cylinder with axis parallel to an in-plane direction. (a) Final ABAQUS FE mesh obtained with the proposed model. (b) Photograph of the final experimental cross-section and EPIC/VPSC simulation results (dashed lines), after Tomé et al. (2001). The arrows indicate the predominant direction of the crystallographic $\langle c \rangle$ -axes.

the specimen deforms mostly in the y -direction and the cross-section of the deformed specimen becomes elliptical. Our simulations predict in-plane expansion of 22% and out-of-plane expansion of 6% (or an ovalization long/short radii = 1.19), which agrees very well with the experimental results reported in Tomé et al. (2001). It is worth noting that under the assumption of isotropic hardening and for fixed values of the anisotropy coefficients (i.e. texture evolution was neglected and the anisotropy coefficients for any pre-strain level were set equal to the values of L obtained based on VPSC yield stresses calculated by probing the 0.2% pre-strained polycrystal in different directions), the predicted expansions would have been of 27% in-plane and 1% out-of-plane. This clearly implies that a good agreement with the experimental results can be obtained only if the changes in anisotropy induced by texture evolution (in this case, a *decrease* in plastic anisotropy) is taken into account. Fig. 2a shows the final ABAQUS FE mesh. The photograph of the final experimental cross-section shape and the superimposed simulation result (obtained using the FE program EPIC directly linked to the VPSC code) are shown in Fig. 2b (simulation and data after Tomé et al., 2001). The comparison demonstrates that very good agreement with the experimental results can be obtained by using an appropriate initial yield surface representation (CPB06) and a hardening law that accounts for texture evolution.

Next, we have simulated the quasi-static through-thickness compression of the zirconium specimen. Fig. 3 shows the yield stresses obtained with the VPSC code (symbols) for five individual levels of compressive pre-strain (0.2%, 1%, 5%, 25% and 35%) along the through-thickness direction, the corresponding five individual CPB06 yield surfaces for which the coefficients were determined (solid lines), and yield surfaces at intermediate levels of strain obtained by linear interpolation (dashed lines). Note that a description of the evolving yield function up to pre-strain levels of around 35% was enough for the 28% strain quasi-static TT compression simulation below.

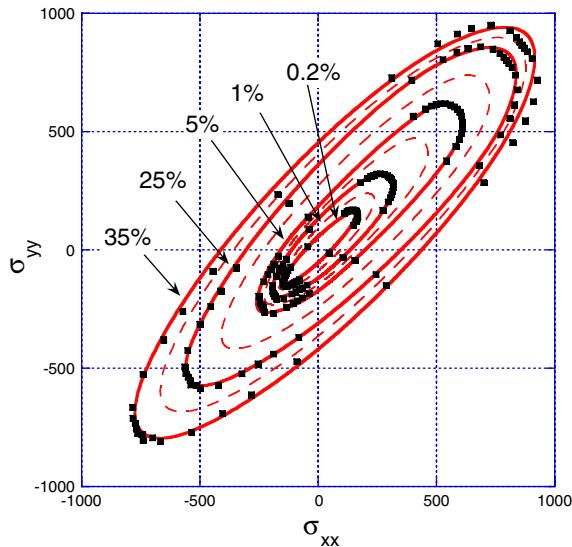


Fig. 3. Theoretical yield surface evolution for a zirconium clock-rolled plate during through-thickness compression for various levels of pre-strain. Solid lines: CPB06 yield surfaces corresponding to fixed pre-strain levels, determined using the VPSC code (symbols). Dashed lines: CPB06 yield surfaces for intermediate pre-strain levels obtained by linear interpolation.

Table 2

CPB06 yield function coefficients corresponding to various pre-strain levels for uniaxial compression of clock-rolled zirconium along the through-thickness direction

	k	L_{12}	L_{13}	L_{22}	L_{23}	L_{33}	L_{44}	L_{55}	L_{66}
0.2%	0.07	2.883	1.875	1.252	1.965	1.204	0.989	1.075	3.956
1%	0.23	2.964	1.556	0.803	1.476	0.433	1.152	1.173	3.313
5%	0.40	2.652	1.619	0.813	1.541	0.583	0.988	1.127	2.858
25%	0.19	3.348	1.575	1.039	1.525	0.603	1.883	2.081	3.391
35%	0.08	3.272	1.524	1.120	1.471	0.641	2.122	2.312	3.847

For all levels of effective plastic strain: $a = 2$ and $L_{11} = 1.0$.

The numerical values of the anisotropy coefficients for CPB06 corresponding to each individual level of pre-strain are listed in Table 2. Note that the CPB06 yield surface evolution associated to deformation induced anisotropy in uniaxial compression is very different than the evolution associated to uniaxial compression in the in-plane direction (cf. Figs. 1 and 3). Through-thickness compression is dominated by slip. Slip-generated crystal rotation would normally result in texture evolution at significant levels of strain. However, in this case the texture is not expected to evolve much from the initial stable strong basal texture. On the other hand, during in-plane compression tensile twinning is easily activated thus producing a strong evolution in texture.

The yield surface evolution depicted in Fig. 3 was in turn used in an ABAQUS FE simulation of compression of a right cylinder of circular cross section and axis parallel to the z -axis up to 28% longitudinal strain, and compared with the experimental results (Tomé et al., 2001) (Fig. 4). Since compression takes place along the axis of symmetry of the sample, the final cross-section remains circular. The proposed model correctly predicts this experimental trend (cf. Fig. 4a and b).

4.2. High strain-rate deformation of zirconium

Controlled impact tests are used to characterize the high strain-rate mechanical response of metals. Such tests provide results in the 10^4 – 10^5 s⁻¹ strain-rate range, directly

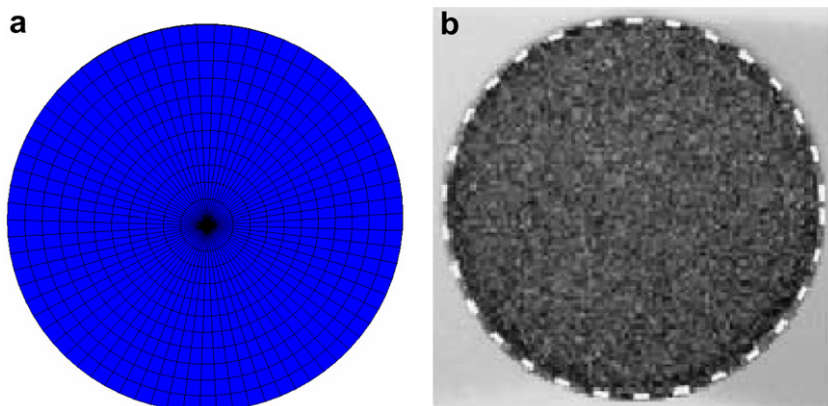


Fig. 4. Cross-sections for quasi-static compression of a zirconium cylinder with axis parallel to the through-thickness direction. (a) Final ABAQUS FE mesh obtained with the proposed model. (b) Photograph of the final experimental cross-section and EPIC/VPSC simulation results (dashed lines), after Tomé et al. (2001).

above that data accessible via Hopkinson Bar techniques and below shock experimentation. One standard approach used is the impact of a right circular cylinder on either a massive anvil (rigid plate) or a receptor rod of identical material. This experiment is commonly called a Taylor impact test (Taylor, 1948). Due to the impact, the rod plastically deforms and shortens causing the material at the impact surface to flow radially outward relative to the rod axis.

Maudlin et al. (1999b) reported results of Taylor cylinder impact tests using in-plane specimens cut from the same zirconium plate described and characterized in the previous section (i.e. cylindrical axes were coincident with in-plane directions). The specimens were 50.8 mm in length and have a length over diameter ratio of 6.67. The anvil was AF1410 steel, heat-treated to a surface hardness of R_c 58 and lapped to a mirror finish. The cylinders were fired using a gas-driven gun at various velocities: 50, 101, 170, and 243 m/s. Only post-test data for the 243 m/s impact velocity were reported. As discussed in Maudlin et al. (1999b), the data set consists of high-resolution scans of the photographed footprint, i.e. the cross-sectional area at the impact interface (on the y - z -plane) and of the photographed side profiles for the major and minor dimensions. From the analysis of the digitized side profiles, axial strain profiles (log strain) as a function of axial position, measured relative to the impact interface, were obtained.

We have applied the proposed elastic-viscoplastic model to the description of the high strain-rate deformation of the clock-rolled zirconium plate at room temperature and compared the simulations with Taylor impact test results reported by Maudlin et al. (1999b). In addition to the yield surface evolution due to plastic deformation, the viscosity coefficient γ and the strain-rate sensitivity parameter m (see Eqs. (2) and (3)) needed to be determined. Results of dynamic in-plane tests performed on the clock-rolled Zr material at strain-rates from 1000/s to 3500/s conducted using a Split Hopkinson Pressure Bar (SHPB) were reported by Kaschner and Gray (2000). Based on these tests, we have determined $\gamma = 2500 \text{ s}^{-1}$ and $m = 7.0$ (see Fig. 5). The constitutive behavior for the in-plane compression corresponding to strains beyond the range of the experimental data was estimated based on polycrystalline calculations.

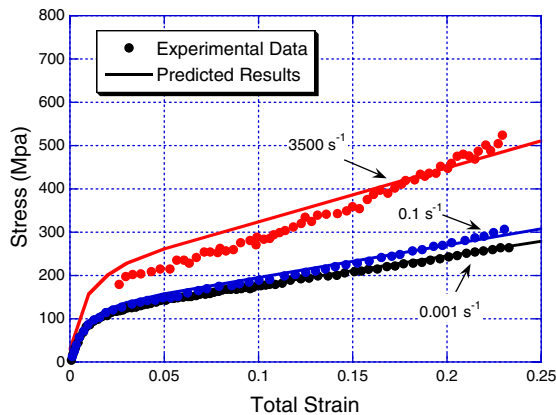


Fig. 5. Stress–strain curves of in-plane compression of clock-rolled zirconium samples for various strain-rates. Symbols: experimental data, after Kaschner and Gray (2000). Lines: simulation results using the proposed elastic-viscoplastic model for $\gamma = 2500 \text{ s}^{-1}$ and $m = 7.0$.

In order to simulate Taylor impact tests of zirconium, the proposed elastic-viscoplastic model was implemented into an ABAQUS explicit user material subroutine. The rate-independent yield surface characterization was the one described in the previous subsection, based on VPSC calculations of the induced anisotropy during quasi-static in-plane compression coupled with CPB06 (see Fig. 3). It should be noted that by making this choice, we have disregarded the possibility of changes in the combination of active deformation mechanisms at single crystal level as strain-rate increases. For comparison purposes, simulations under the assumption of isotropic hardening and anisotropy coefficients set equal to the anisotropy coefficients corresponding to 0.2% pre-strain (texture evolution neglected) were also carried out.

The zirconium cylinder was modeled using 2117 ABAQUS C3D8R linear brick elements with free boundary conditions. The anvil target was modeled as an analytical rigid surface. Simulations were done for the impact velocity of 243 m/s. The step size used to simulate the event was $\Delta t = 2 \times 10^{-8}$ s. Calculations were performed for 90 μ s, at which time the specimen had rebound off of the target and all plastic deformation had ceased. Fig. 6 shows a comparison between the experimental and simulated logarithmic strain profile along the major and minor axes of the post-test specimen. The strains along the major and minor elliptical axes, which are both zero at large z , accumulate at different rates as z decreases. A good agreement with the experimental data is observed. Fig. 7 depicts a visual comparison between the simulated and experimental major and minor profiles and foot-

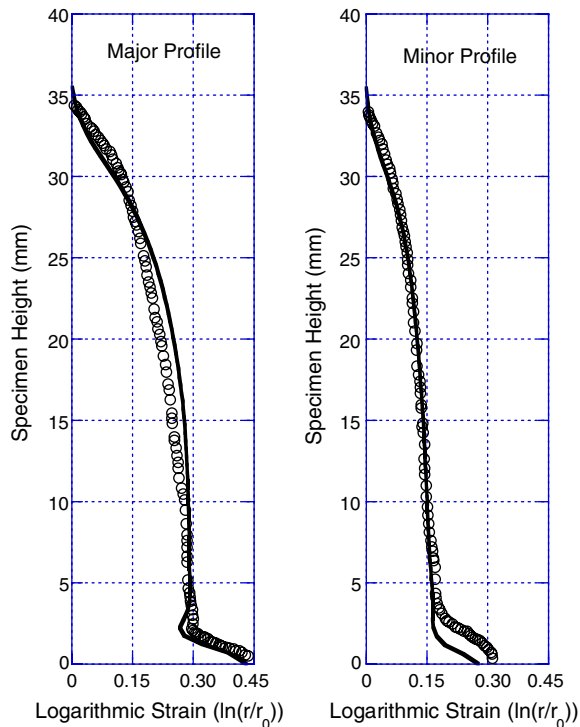


Fig. 6. Comparison of theoretical (lines) and experimental (symbols) logarithmic strain profiles of the post-test zirconium Taylor impact specimen. Data after Maudlin et al. (1999b).

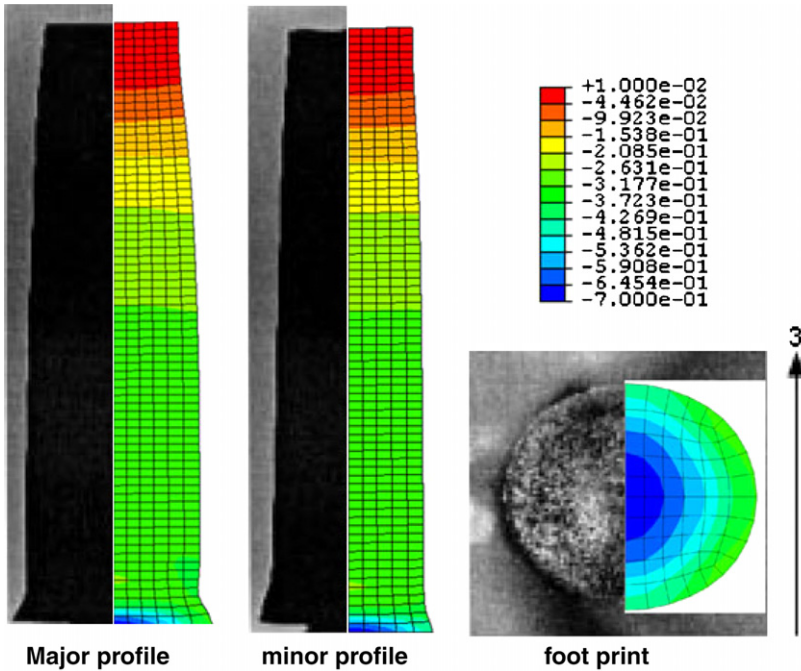


Fig. 7. Comparison of the simulated (with contours of axial plastic strain) and experimental cross-sections of the post-test zirconium Taylor impact experiment for the major profile, the minor profile, and the footprint. Data after Maudlin et al. (1999b).

print of the post-test specimen. The slight differences between the experimental data and the simulation results are most likely related to temperature effects which were not taken into consideration in the simulations because experimental data was not available. Note that the geometry of the footprint of the specimen clearly indicates a decrease in anisotropy (the ratio of major to minor diameter is ≈ 1.1). This is due to the large twinned volume fraction resulting from strains of around 60–70% at the impact section (see strain levels in Fig. 7) which tends to decrease the intensity of the texture (as already seen in Fig. 1 and discussed in Section 4.1).

As discussed earlier in the quasi-static case, the consideration of a hardening law that accounts for texture evolution is essential to obtain the good agreement with the experimental results. Fig. 8 shows a comparison between experimental minor and major profiles of the post-test specimen and those calculated using isotropic hardening and fixed values for the anisotropy coefficients corresponding to 0.2% pre-strain. It is evident that the effects of substantial twinning activity can be captured only by a hardening law that reflects the evolution of texture.

4.3. High strain-rate deformation of tantalum

The anisotropic elastic-viscoplastic model was originally developed to capture the anisotropic, asymmetric hardening behavior of hcp metals. The static yield surface in this model is the CPB06 yield surface. However, the CPB06 criterion can be also used to rep-

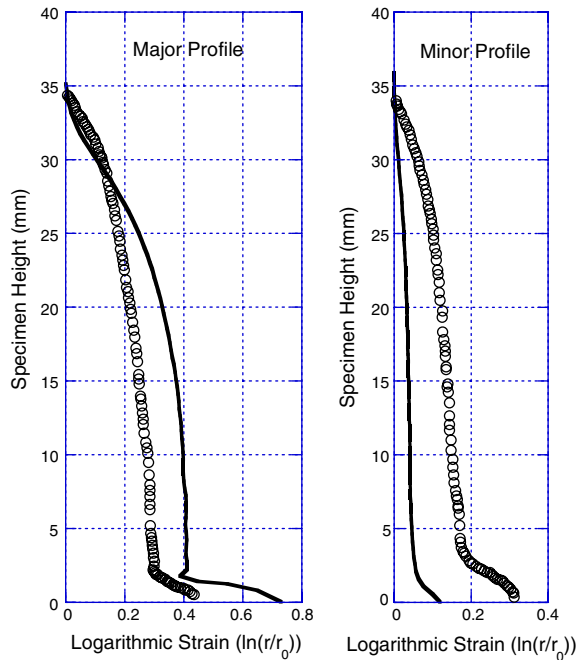


Fig. 8. Comparison of theoretical (lines) and experimental (symbols) logarithmic strain profiles of the post-test zirconium Taylor impact specimen. Simulation were performed with an isotropic hardening law. Data after Maudlin et al. (1999b).

resent the yielding behavior of a material with cubic crystallographic structure deforming solely by slip by simply setting the strength-differential coefficient k to zero. In this section, we apply the proposed formulation to the description of the anisotropy of a bcc tantalum sheet (obtained by unidirectional rolling and displaying a near-orthotropic texture) subjected to high strain-rate and large plastic deformations (data after Maudlin et al., 1999a,b).

Unlike for the previously studied clock-rolled zirconium, in this case there was no sufficient experimental data available to quantify the deformation induced anisotropy using VPSC simulations (i.e. no data based on which we could determine the parameters involved in the VPSC model were available). Therefore, to estimate the coefficients involved in the macroscopic CPB06 yield criterion, we have used the values of yield stresses in different directions reported by Maudlin et al. (1999a,b). The numerical values of the CPB06 coefficients are listed in Table 3. Moreover, due to lack of information regarding the yield behavior in pure shear, it was assumed a value equal to 0.577 times the yield stress in uniaxial tension along the rolling direction. Fig. 9 shows the projection in the biaxial plane of the CPB06 orthotropic yield surface for tantalum (solid lines) together with the yield stresses (symbols) calculated by Maudlin et al. (1999a,b) using a Taylor–Bishop–Hill (TBH) polycrystal model.

Uniaxial compression test results at various strain-rates and temperatures were reported for tantalum specimens cut from the same rolled plate. Results of Split-Hopkinson bar tests performed at different temperatures in the range 200–1000 °C and for strain-rates in the range 2800–3900 s⁻¹ have shown that the compressive response depends on the

Table 3

CPB06 yield function coefficients corresponding to rolled tantalum; $a = 2$ and $L_{11} = 1.0$

k	L_{12}	L_{13}	L_{22}	L_{23}	L_{33}
0	-0.1911	-0.0687	1.0411	0.0067	1.1366

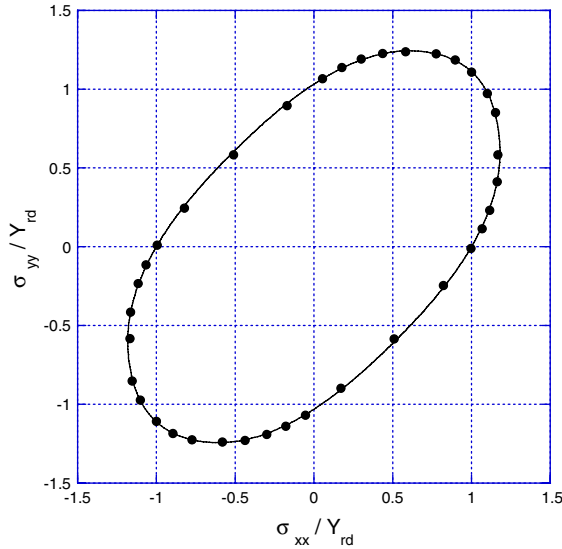


Fig. 9. Line: CPB06 yield surface corresponding to a rolled sheet of tantalum. Symbols: yield stress points predicted with the Taylor–Bishop–Hill approach. Stresses are normalized about the yield stress in the x -direction (rolling direction). Data after Maudlin et al. (1999a,b).

strain-rate and temperature. The yield stress was found to increase with increasing strain-rate and decreasing temperature. To capture the effect of temperature on the compressive yield stress of tantalum we used a Johnson–Cook type hardening law (Johnson and Cook, 1983):

$$Y(\bar{\epsilon}_{vp}, T) = Y_0(\bar{\epsilon}_{vp}) \left[1 - \left(\frac{T - T_{rm}}{T_{melt} - T_{rm}} \right)^{tm} \right] \quad (25)$$

In Eq. (25), $Y_0(\bar{\epsilon}_{vp})$ is the rate-independent hardening law at room temperature, T_{rm} is the room temperature (typically 25 °C), T_{melt} is the melting temperature, and tm is a material constant. For tantalum, $T_{melt} = 2977$ °C, while a value of 0.42 for the exponent tm gives an overall good approximation of the experimental data. Assuming that all mechanical work is converted into heat, from the energy equation (Malvern, 1969) the temperature rise due to mechanical deformation is:

$$\Delta T = \frac{\boldsymbol{\sigma} : \Delta \boldsymbol{\epsilon}_{vp}}{\rho c_p} \quad (26)$$

For tantalum, $\rho = 16,640$ kg/m³, $c_p = 140$ J/kg K. Furthermore, using the available data, a viscosity $\gamma = 1500$ s⁻¹ and a strain-rate sensitivity parameter $m = 5.0$ (see Eq. (2)) were determined.

Next, we evaluated the predictive capability of the present model to simulate the severe geometry changes of the tantalum Taylor specimens reported by Maudlin et al. (1999a,b). The cylinders were 38.1 mm long and 7.6 mm in diameter. The longitudinal axis of the specimen was either parallel to the rolling direction (y) or transverse direction (x). Only results on specimens having the longitudinal axis parallel to the rolling direction were reported. The cylinders were launched using a powder gun. The velocity of the cylinders measured using both pressure transducers and parallel laser beams were $175 \text{ m/s} \pm 3 \text{ m/s}$. The anvil target was made of steel. Metallographic analysis of the pre- and post-test specimens showed negligible texture evolution. Therefore, the experiment was modeled assuming isotropic hardening. Because the material was orthotropic, only a quarter section was modeled using 8170 ABAQUS C3D8R linear brick elements with free boundary conditions and an initial velocity of 175 m/s . The step size used to simulate the event was $\Delta t = 2 \times 10^{-8} \text{ s}$ and was conducted until $100 \mu\text{s}$. At $100 \mu\text{s}$ the specimen had rebound off of the target, and all plastic deformation had ceased. The anvil target was modeled as an analytical rigid surface. A higher number of elements were used for the tantalum simulations as compared to the zirconium simulations because the tantalum specimen undergoes larger deformations (for tantalum at $z = 0$, the strain along the major and minor dimensions were of 87% and 70%, respectively while for zirconium the values of the strains at $z = 0$ were of 44% and 31%, respectively). Axial strain profiles for both the major and minor sides of the deformed specimens (cylinder axis parallel to the rolling direction) in comparison with experiments are shown in Fig. 10. Very good agreement is observed. The simulated and experimental footprints of the post test specimen are shown in Fig. 11. The data shown in Figs. 10 and 11 are the results from three separate experiments conducted for different specimens under the same conditions. The simulated and experimental post-test specimens are visually compared in Fig. 12. In

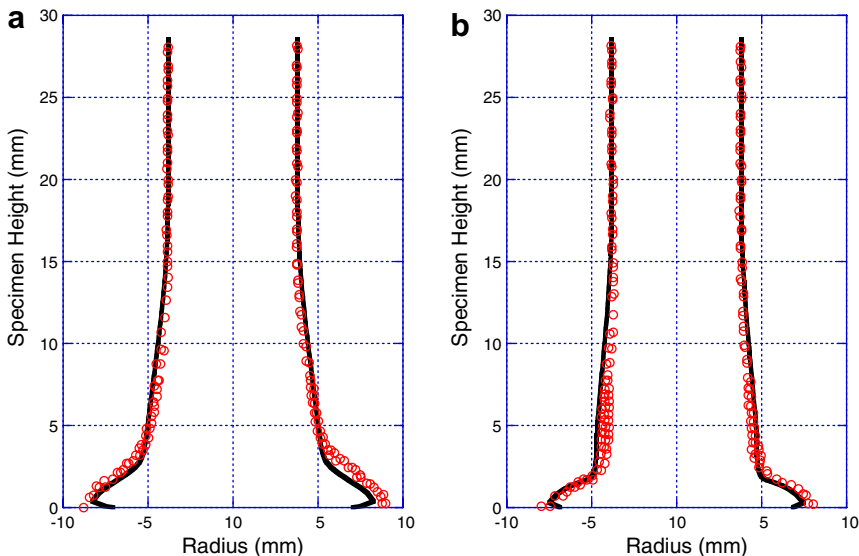


Fig. 10. (a) Major and (b) minor profiles of the tantalum Taylor impact specimen. Solid lines represent simulation results, symbols represent experimental data. Data after Maudlin et al. (1999a,b).

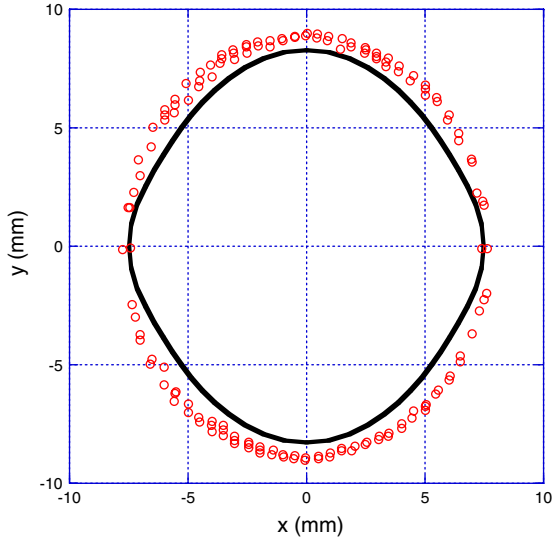


Fig. 11. Footprint of the tantalum Taylor impact specimen. Solid lines represent simulation results, symbols represent experimental data. Data after Maudlin et al. (1999a,b).

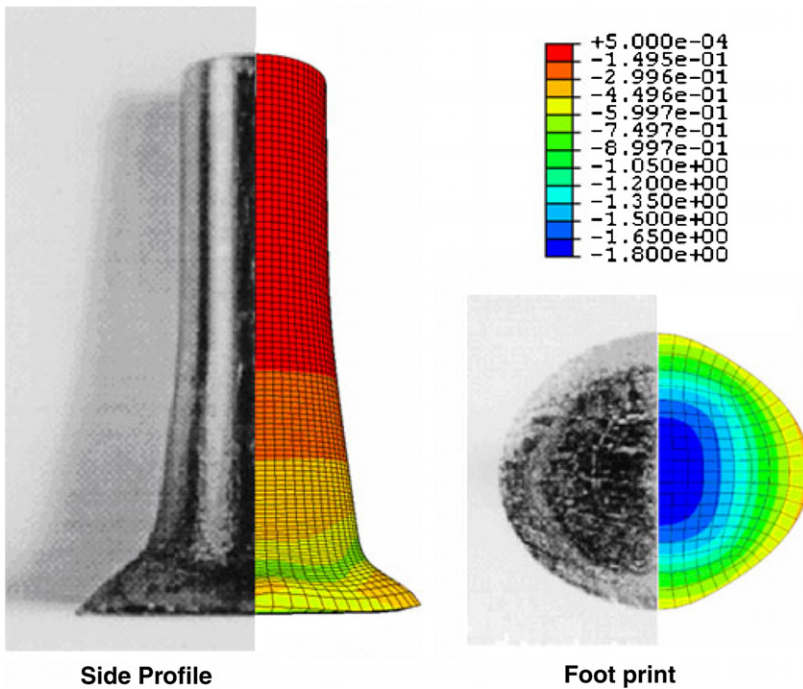


Fig. 12. Comparison between simulated (with contours of axial plastic strain) and experimental tantalum Taylor impact specimens. Photographs of the post-test specimen after Maudlin et al. (1999a,b).

Maudlin et al. (1999b), the same tests were simulated by introducing anisotropy through direct link between the Taylor–Bishop–Hill polycrystal model and the FE code EPIC, assuming the presence of a polycrystal at each integration point. Their results were also in very good agreement with the experimental data. However, Figs. 10–12 clearly demonstrate that very accurate results can also be obtained with the present formulation, at a fraction of the computation time.

5. Conclusions

A macroscopic anisotropic elastic-viscoplastic model that captures the influence of evolving texture on the mechanical response of textured metals for both quasi-static and dynamic loading conditions was proposed. Yielding was described using the anisotropic yield function proposed by Cazacu et al. (2006). This yield function can capture simultaneously both anisotropy and tension/compression asymmetry. Moreover, if the parameter associated with strength differential effects is set to zero, the yield function also describes with accuracy yielding of metals with cubic symmetry.

The anisotropy coefficients as well as the size of the elastic domain were considered to be functions of the accumulated plastic strain. To capture the anisotropy induced by texture evolution, a multi-scale methodology consisting in using experimental textures and stress–strain curves, VPSC polycrystalline calculations, and macroscopic scale interpolation techniques was used. The procedure started by fitting the parameters of the polycrystal model to reproduce the mechanical response of the pre-textured material. Next, using this adjusted polycrystal model, the evolution of texture was calculated for fixed pre-strain level along a given deformation path. Then, in order to quantify the induced anisotropy, the pre-strained polycrystal was numerically probed along various directions. The calculated yield stresses along these directions were in turn used to determine the CPB06 coefficients. This procedure was repeated for a finite set of pre-strain levels and linear interpolation was in turn used to obtain the macroscopic yield surfaces corresponding to an arbitrary pre-strain level.

The above procedure was used to model the quasi-static mechanical response of high-purity zirconium. Since the proposed model accounts for the deformation mechanisms associated with a given deformation path, it captured the strong anisotropy and texture evolution produced by twinning which is observed when the material is subjected to in-plane compression. On the other hand, the resulting macroscopic yield surface evolution along through-thickness compression was very different than the one associated with in-plane compression (cf. Figs. 1 and 3). Through-thickness compression is dominated by slip so the texture does not significantly change during loading, whereas during in-plane compression tensile twinning is easily activated, producing a strong texture evolution.

Based on the above model for quasi-static behavior, an overstress type of approach was in turn used to account for rate effects. The resulting elastic-viscoplastic model was applied to the description of the high strain-rate response of low-symmetry (clock-rolled hcp zirconium) and high-symmetry (rolled bcc tantalum) textured metals. The very good agreement between the simulated and experimental post-test geometries of the Taylor-impact specimens in terms of major and minor side profiles and impact footprints proved the ability of the model to describe the striking difference in the evolution of anisotropy between zirconium and tantalum.

Acknowledgements

This work was partially supported through Grant FA8651-05-1-0005 provided by the US Air Force, AFRL/MNAC. The authors thank Drs. Carlos Tome, Paul Maudlin, George Kaschner and Rusty Gray for fruitful discussions and for providing the experimental data used as input and validation of the proposed approach.

References

- ABAQUS Version 6.4 Reference Manuals, 2003. Pawtucket, RI.
- Anand, L., Balasubramanian, S., Kothari, M., 1997. Constitutive modeling of polycrystalline metals at large Strains: application to deformation processing. In: Teodosiu, C. (Ed.), *Large Plastic Deformation of Crystalline Aggregates, CISM Courses and Lectures (International Center for Mechanical Sciences)*, vol. 376. Springer, Wien New York.
- Bishop, J.W.F., Hill, R., 1951. A theoretical deviation of the plastic properties of a polycrystalline face-centered metal. *Phil. Mag. Ser. 742*, 1298–1307.
- Cazacu, O., Barlat, F., 2003. Application of representation theory to describe yielding of anisotropic aluminum alloys. *Int. J. Eng. Sci.* 41, 1367–1385.
- Cazacu, O., Plunkett, B., Barlat, F., 2006. Orthotropic yield criterion for hexagonal closed packed metals. *Int. J. Plasticity* 22, 1171–1194.
- Henrie, B.L., Mason, T.A., Hansen, B.L., 2004. A semiautomated electron backscatter diffraction technique for extracting reliable twin statistics. *Metall. Mater. Trans. A* 35, 3745–3751.
- Hill, R., 1987. Constitutive dual potentials in classical plasticity. *J. Mech. Phys. Solids* 15, 79–95.
- Johnson, G.R., Cook, W.H., 1983. A constitutive model and data for metals subjected to large strains, high strain rates, and high temperatures. In: *Proceedings of Seventh International Symposium on Ballistics*.
- Kaschner, G.C., Gray, G.T., 2000. The influence of crystallographic texture and interstitial impurities on the mechanical behavior of zirconium. *Metall. Mater. Trans. A*, 31, 1997–2003.
- Lebensohn, R.A., Tomé, C.N., 1993. A self-consistent anisotropic approach for the simulation of plastic deformation and texture development of polycrystals: Application to zirconium alloys. *Acta Metall. Mater.* 41, 2611–2624.
- Malvern, L.E., 1969. *Introduction to the mechanics of continuous medium*. Prentice Hall, Inc., Upper Saddle River, NJ.
- Maudlin, P.J., Bingert, J.F., House, J.W., Chen, S.R., 1999a. On the modeling of the Taylor cylinder impact test for orthotropic textured materials: experiments and simulations. *Int. J. Plasticity* 15, 139–166.
- Maudlin, P.J., Gray, T.G., Cady, C.M., Kaschner, C.G., 1999b. High rate material modeling and validation using the Taylor cylinder impact test. *Phil Trans R. Soc.* 357, 1707–1729.
- Perzyna, P., 1966. *Fundamental problems in viscoplasticity*. Recent Advances in Applied Mechanics, vol. 9. Academic Press, New York, pp. 243–377.
- Plunkett, B., Lebensohn, R.A., Cazacu, O., Barlat, F., 2006. Evolving yield function of hexagonal materials taking into account texture development and anisotropic hardening. *Acta Mater.* 54, 4159–4169.
- Salem, A.A., Kalidindi, S.R., Semiatin, S.L., 2005. Strain hardening due to deformation twinning in a-titanium: constitutive relations and crystal-plasticity modeling. *Acta Mater.* 53, 3495–3502.
- Simo, J.C., Hughes, T.J.R., 1998. *Computational Inelasticity*. Springer-Verlag, New York.
- Soare, S., Barlat, F., Cazacu, O., Yoon, J.W., 2007. Application of a recently proposed yield function to sheet forming. In: Banabic, D. (Ed.), *Advanced Methods in Material Forming*. Springer-Verlag (in press).
- Staroselsky, A., Anand, L., 2003. A constitutive model for hcp materials deforming by slip and twinning: application to magnesium alloy AZ31B. *Int. J. Plasticity* 19, 1843–1864.
- Taylor, G.I., 1948. The use of flat-ended projectiles for determining dynamic yield stress. *Proc Royal Soc. A* 194, 289–299.
- Tomé, C.N., Lebensohn, R.A., 2004. Self-consistent homogenization methods for texture and anisotropy. In: Raabe, D., Roters, F., Barlat, F., Chen, L.-Q. (Eds.), *Continuum Scale Simulation of Engineering Materials*. Wiley-VCH, Weinheim, pp. 473–497 (Chapter 8).
- Tomé, C.N., Maudlin, P.J., Lebensohn, R.A., Kaschner, G.C., 2001. Mechanical response of zirconium-I. Derivation of a polycrystal constitutive law and finite element analysis. *Acta Mater.* 49, 3085–3096.

- Wang, W.M., Sluys, L.J., De Borst, R., 1997. Viscoplasticity for instabilities due to strain softening and strain-rate softening. *Int. J. Numer. Meth. Eng.* 40, 3839–3864.
- Yoon, J.W., Yang, D.Y., Chung, K., Barlat, F., 1999. A general elasto-plastic finite element formulation based on incremental deformation theory for planar anisotropy and its application to sheet metal forming. *Int. J. Plasticity* 15, 35–67.
- Yoon, J.W., Barlat, F., Dick, R.E., Karabin, M.E., 2006. Prediction of six or eight ears in a drawn cup based on a new anisotropic yield function. *Int. J. Plasticity* 22, 174–193.